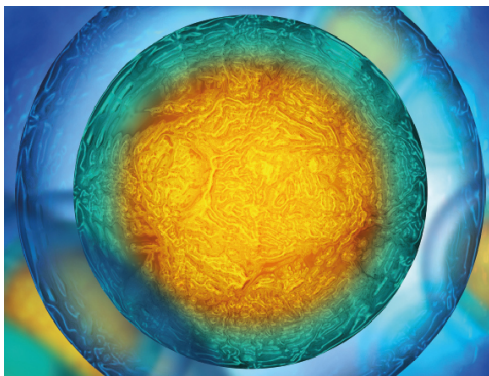**PAPER • OPEN ACCESS**

Engineering the early bone metastatic niche through human vascularized immuno bone minitissues

To cite this article: Maria Vittoria Colombo *et al* 2021 *Biofabrication* **13** 035036

View the article online for updates and enhancements.

Biophysical Society **IOP | ebooks™**

Your publishing choice in all areas of biophysics research.

Start exploring the collection–download the first chapter of every title for free.

Biofabrication

PAPER

Engineering the early bone metastatic niche through human vascularized immuno bone minitissues

Maria Vittoria Colombo[1,2,§] [ID], Simone Bersini[1,§] [ID], Chiara Arrigoni[1] [ID], Mara Gilardi[3], Veronica Sansoni[4], Enrico Ragni[5], Gabriele Candiani[2] [ID], Giovanni Lombardi[4,8] [ID] and Matteo Moretti[1,6,7,*] [ID]

[1] Regenerative Medicine Technologies Laboratory, Ente Ospedaliero Cantonale, 6900 Lugano, Switzerland
[2] Biocompatibility and Cell Culture Laboratory 'BioCell', Department of Chemistry, Materials and Chemical Engineering 'Giulio Natta', Politecnico di Milano, 20133 Milano, Italy
[3] Institute of Pathology, University Hospital of Basel, Basel 4056, Switzerland
[4] IRCCS Istituto Ortopedico Galeazzi, Laboratory of Experimental Biochemistry and Molecular Biology, 20161 Milano, Italy
[5] IRCCS Istituto Ortopedico Galeazzi, Orthopedic Biotechnology Lab, 20161 Milano, Italy
[6] IRCCS Istituto Ortopedico Galeazzi, Cell and Tissue Engineering Laboratory, 20161 Milano, Italy
[7] Faculty of Biomedical Sciences, Università della Svizzera Italiana, 6900 Lugano, Switzerland
[8] Department of Athletics, Strength and Conditioning, Poznań University of Physical Education, Poznań 61-871, Poland
[§] Equally contributing.
[*] Author to whom any correspondence should be addressed.

E-mail: matteo.moretti@eoc.ch

Abstract

Bone metastases occur in 65%–80% advanced breast cancer patients. Although significant progresses have been made in understanding the biological mechanisms driving the bone metastatic cascade, traditional 2D *in vitro* models and animal studies are not effectively reproducing breast cancer cells (CCs) interactions with the bone microenvironment and suffer from species-specific differences, respectively. Moreover, simplified *in vitro* models cannot realistically estimate drug anti-tumoral properties and side effects, hence leading to pre-clinical testing frequent failures. To solve this issue, a 3D metastatic bone minitissue (MBm) is designed with embedded human osteoblasts, osteoclasts, bone-resident macrophages, endothelial cells and breast CCs. This minitissue recapitulates key features of the bone metastatic niche, including the alteration of macrophage polarization and microvascular architecture, along with the induction of CC micrometastases and osteomimicry. The minitissue reflects breast CC organ-specific metastatization to bone compared to a muscle minitissue. Finally, two FDA approved drugs, doxorubicin and rapamycin, have been tested showing that the dose required to impair CC growth is significantly higher in the MBm compared to a simpler CC monoculture minitissue. The MBm allows the investigation of metastasis key biological features and represents a reliable tool to better predict drug effects on the metastatic bone microenvironment.

1. Introduction

The metastatic dissemination of specific primary tumors follows a distribution pattern described by the 'seed and soil' hypothesis [1]. In this context, metastasizing breast cancer cells (CCs) preferentially colonize the bone with 65%–80% advanced breast cancer patients presenting incurable bone metastases associated with a poor prognosis [2].

Breast cancer mainly induces osteolytic bone metastases which are characterized by a pathological activation of osteoclasts (OCs) that unbalance the bone remodeling process and establish the so-called 'vicious cycle' [3]. In this process, CCs and bone cells concur to the deregulation of key bone signaling factors, hence stimulating tumor growth [4, 5]. Moreover, CCs recruit and educate a population of tumor-associated macrophages (TAMs), which foster immunosuppression, contribute to bone remodeling and promote abnormal angiogenesis [6]. Furthermore, the vascular niche plays a fundamental role in bone metastases. Indeed, the morphological and

adhesive properties of the bone vasculature seem to promote the invasion of breast CCs to the bone and to activate dormancy programs in disseminated tumor cells [7].

Understanding the interactions between CCs and stromal cells in this complex and heterogeneous microenvironment represents a critical challenge to stop or prevent bone metastases. In this context, animal models allow to analyze the formation of bone metastases in a living organism. However, they suffer from species-specific differences compared to human tissues, including immune cells that do not fully mimic their human counterparts [8]. On the other hand, traditional two-dimensional (2D) *in vitro* models consist of monolayer monocultures or co-cultures which do not allow to grow cells in the tissue-specific architecture characterizing human tissues, hence leading to non-physiological cell-to-cell communications [9]. Furthermore, traditional 2D models cannot faithfully predict both the main and side effects of drugs in a given tissue. The inadequacy of these models hindered the finding of new therapies and contributed to the failure of several cancer treatments [10]. Multicellular three-dimensional (3D) models partially overcome the limitations of monolayer cultures by promoting a more physiological interaction of different cell types that better mimics the metastatic microenvironment, whereby CCs interact with osteoblasts (OBs), OCs, bone resident macrophages and endothelial cells (ECs), and deregulate the tissue homeostasis [11, 12]. Previous studies have reported the generation of 3D *in vitro* models which replicate the process of bone remodeling by including bone-forming OBs and bone-resorbing OCs [13, 14]. Other studies highlighted the importance of the vascular fraction for differentiation of mesenchymal stem cells (MSCs) in OBs and promotion of osteogenesis and mineralization of the tissue construct under static or flow conditions [15–17]. However, only a few studies reported the combined use of more than two cell types or included hydroxyapatite or calcium phosphate nanoparticles to promote matrix deposition [18–20]. Most bone metastasis studies focused on the interaction of breast CCs with a single bone cell type (i.e. OBs or OCs) or on the interplay between ECs and different breast CC lines [21–23]. At the same time, the interaction of TAMs with breast CCs was mainly analyzed in the context of the primary tumor or during the intravasation process [24–26].

Overall, replicating the cellular complexity characterizing the bone metastatic microenvironment still remains an open challenge limiting the possibility to test novel drugs and analyze the contribution of stromal cells in the metastatic progression. We previously developed 3D bone remodeling models which allowed us to generate customized microvascular networks based on the combination of biochemical and physical parameters [20, 27]. Here, we propose an attempt to introduce all the main cell types involved in breast cancer bone metastases (i.e. CCs, OBs, OCs, ECs and bone resident macrophages) to characterize how key cell–cell interactions contribute to the formation of the early bone metastatic microenvironment and its response to anti-metastatic drugs. We showed that CCs in a complex early metastatic bone niche were able to mimic features of OCs, including expression of OC markers and bone resorption activity, and to activate M0 macrophages and alter the balance between M1 and M2 cells. We compared the bone microenvironment with a skeletal muscle microenvironment, which is not a site of breast cancer metastasis, and we investigated if the inhibition of CC growth was due to the presence of specific soluble signals secreted by muscle cells (e.g. adenosine) [28]. We demonstrated that the presence of a complex early metastatic bone microenvironment impacts the outcome of anti-cancer drug treatments showing that cellular complexity is an essential feature to better predict the effect of drug candidates on bone metastatic progression.

2. Materials and methods

2.1. Cell culture

OCs and macrophages were differentiated from circulating monocytes isolated from buffy coat following previously optimized protocols [20]. Monocytes were cultured in RPMI (Life Technologies) containing 10% fetal bovine serum (FBS, Fisher Scientific), 1% penicillin-streptomycin-glutamine (PSG, Life Technologies), 1% amphotericin B and 25 ng ml^{-1} macrophage colony stimulating factor (M-CSF, Peprotech) to promote monocyte-derived macrophage differentiation (M0). After 24 h, attached M0 were cultured in the same medium while OCs were differentiated from M0 by adding 50 ng ml^{-1} receptor activator of NF-κB ligand (RANKL, Peprotech) to the cell culture medium. Adult human osteoblasts (OBs, Sigma) were cultured in Dulbecco's Modified Eagle Medium (DMEM, Life Technologies) with addition of 15% FBS, 1% PSG and 1% amphotericin B. Primary red fluorescent protein-transfected human umbilical vein endothelial cells were purchased from Angio-Proteomie, cultured in endothelial growth medium (EGM)-2 (Lonza) with addition of 3% FBS. Green fluorescent protein-transfected MDA-231 breast CCs were cultured in DMEM supplemented with 10% FBS and 1% PSG. Immortalized human myoblasts (MYs) were cultured in DMEM:199 (4:1) (Life Technologies) supplemented with 15% FBS, 2% HEPES (Life Technologies), 1% PSG, 0.03 μg ml^{-1} ZnSO$_4$ (Sigma), 1.4 μg ml^{-1} vitamin B12 (Sigma), 0.055 μg ml^{-1} dexamethasone (Sigma), 1% sodium pyruvate (Life technologies), 2.5 ng ml^{-1} hepatocyte growth factor (Peprotech) and 10 ng ml^{-1} fibroblast growth factor (FGF, Peprotech). Muscle-specific

fibroblasts (mFs) were cultured in DMEM supplemented with 10% FBS, 1% PSG and 1% FGF.

2.2. Hydrogel minitissue fabrication

3D arch-shaped poly-methyl-methacrylate (PMMA) masks with 5 mm depth and two 2×2 mm^2 openings were designed and optimized through computational simulations, as previously reported [27] to allow standardized matrix injection, long-term culture and cell recovery. In our previous study, we demonstrated how this design allowed to generate microvascular networks with customized features (e.g. network length, number of branches) in a bone-mimicking model.

Following CAD design, PMMA cages with two open faces were fabricated by laser cutting and bonded to 100 μm thick glass coverslips (figure (A)). Masks were sterilized with 70% ethanol. Polymerized gels with embedded cell suspensions were encased in the masks and daily monitored during the maturation of the tissue.

Four different minitissues were designed (figures (B) and (C)): healthy bone minitissue (Bm) containing ECs, OBs and OCs; metastatic bone minitissue (MBm) containing ECs, OBs, OCs and CCs; other two minitissues were developed embedding resident M0 starting from Bm and MBm, called respectively immune bone minitissue (IBm) and metastatic immune bone minitissue (MIBm). Cells were embedded in 2.5 mg ml^{-1} fibrin hydrogels (Sigma) with the following final concentrations: 3×10^6 cells ml^{-1} ECs, 1.5×10^6 cells ml^{-1} OBs and 0.15×10^6 cells ml^{-1} OCs and M0, based on previous studies [27]. CC density was chosen based on preliminary experiments not reported in this study. Briefly, CCs were embedded in 2.5 mg ml^{-1} fibrin hydrogels with three different final concentrations (i.e. 0.01×10^6 cells ml^{-1}, 0.15×10^6 cells ml^{-1}, and 0.5×10^6 cells ml^{-1}). We selected 0.15×10^6 cells ml^{-1} as the best compromise for both matrix stability and CC proliferation over 7 d. Two muscle minitissues were developed: a healthy muscle minitissue (Mm) embedding in 2.5 mg ml^{-1} fibrin gel ECs (seeding concentration: 3×10^6 cells ml^{-1}), MYs (seeding concentration: 1.5×10^6 cells ml^{-1}) and mFs (seeding concentration: 0.15×10^6 cells ml^{-1}); the Mm was then enriched with CCs (seeding concentration: 0.15×10^6 cells ml^{-1}) to generate a metastatic muscle minitissue (MMm). Hydrogels were polymerized within humidity boxes at 37° for 20 min and cultured in EGM-2 with the addition of 3% FBS until day 7 with one medium change at day 3.

2.3. Drug treatment

The drug treatments were performed on the MIBm and on a minitissue of CCs embedded in 2.5 mg ml^{-1} fibrin hydrogel (seeding concentration: 0.15×10^6 cells ml^{-1}), labelled cancer control minitissue (CCm). Samples were prepared as previously explained and the drugs were added to the culture medium at day 3. Samples were treated with 1 μM doxorubicin (DOX) or with 2 nM or 20 nM rapamycin and kept in culture until day 5 in DOX and day 7 in rapamycin [29, 30].

Other two assays were performed: the MIBm was treated with 10 μM or 100 μM adenosine, while the MMm was treated with 1 μM PSB-10 (i.e. antagonist of the A$_3$ adenosine receptor) [31, 32]. In those assays, the compounds were added starting from day 0, the culture medium was changed at day 3 and the tissue constructs were kept in culture until day 7.

To evaluate drug efficacy, we analyzed area fraction of CCs. Images of CCs were converted into binary format using a threshold which maintained CC signal. We measured area fraction of the binary images of at least three samples for each condition. Finally, statistical analyses of CC area fraction were performed to evaluate CC growth related to drug treatment.

2.4. Immunofluorescence

Immunofluorescent staining for RANK (mouse anti-human, Santa Cruz Biotechnology, 1:50), collagen type I (rabbit anti-human, Abcam, 1:500), osteocalcin (rabbit anti-human, Abcam, 1:100), OPN (rabbit anti-human, Abcam, 1:100), tartrate resistant acid phosphatase (TRAP) (mouse anti-human, Thermo Scientific, 1:100), HLA-DR (mouse anti-human, Biolegend, 5 μg ml^{-1}), CD163 (rabbit anti-human, Santa Cruz Biotechnology, 1:50), intercellular adhesion molecule (ICAM)-1 (rat anti-human, Thermo Scientific, 1:200), Ki67 (rabbit anti-human, Thermo Scientific, 1:150) were performed following cell fixation with 2% paraformaldehyde, membrane permeabilization with 0.1% Triton-X 100 and overnight incubation with 5% bovine serum albumin (BSA) at 4 °C. Following 24 h primary antibody incubation (extruded 3D samples) or overnight incubation (2D samples) at 4 °C, samples were washed in phosphate buffered saline (PBS, Life Technologies) and secondary antibodies were incubated following the same protocol applied for primary antibodies. More in detail, we used goat anti-rabbit or goat anti-mouse Alexa Fluor 647 (Life Technologies, 1:200). If required, samples were stained with DAPI (300 nM final concentration) and Vybrant™ (Life Technologies).

2.5. TRAP activity assay

The TRAP activity assay was performed comparing 14 d differentiated OCs and undifferentiated OCs using a commercial acid phosphatase colorimetric assay kit (Abcam, Cambridge, UK). The assay allows to detect the μU of acid phosphatase (AP) in the sample using p-nitrophenyl phosphate (pNPP) as substrate. In presence of AP enzyme, pNPP is dephosphorylated and turns yellow (wavelength $\lambda = 405$ nm). Absorbance levels were evaluated by

VICTOR® X³Multilabel Counter (Perkin Elmer, Inc., MA, USA) and statistical analyses were performed.

2.6. Inflammatory biomarker measurements
Culture media were collected at day 2 and day 7 and immediately frozen at -80 °C. A panel of 37 key inflammatory biomarkers has been assayed through a high sensitivity multiplex bead-based immuno-fluorescent assay (Bio-Plex Pro™ Human Inflammation Panel 1, 37-Plex, Bio-Rad Laboratories, Inc., Hercules, CA, USA) on a MagPix™ Luminex System (Bio-Rad Laboratories, Inc.) following manufacturer instructions. Osteoprotegerin (OPG) and RANKL concentrations were measured by enzyme-linked immunosorbent assay. OPG (Raybiotech, Peachtree Corners, GA, USA) and RANKL (Boster Biological Technology, Pleasanton, CA, USA) assays have a sensitivity of 1 pg ml^{-1} and <10 pg ml^{-1} respectively. All samples were tested in duplicate.

2.7. Bone resorption assay
Dentine slices (IDS, The Boldons, UK) were prepared by placing them in 70% ethanol for 15 min and washed twice with dd-H$_2$O to remove residues. CCs treated or not with RANKL were seeded on dentine slices in 96 wells plate at a concentration of 780 cells/well and cultured for 14 d in EGM-2. Culture medium was changed twice a week. Dentine slices were then decellularized with bleach and the bone resorption lacunae were stained with toluidine blue. Images were taken at the stereomicroscope and the quantity of resorption pits was scored using ImageJ software. Images were converted into binary using a threshold that captured all the resorption pits. At least four regions of interests (ROIs) for each sample were considered. The area fraction was then analyzed in both conditions.

2.8. Cell cycle analysis
Cell cycle analysis was performed on samples treated with doxorubicin to investigate the effect of the drug on CC cycle. At day 7 samples were extruded and fibrin was degraded with nattokinase (1 mg ml^{-1} in PBS) at 37 °C for 1 h. Cells were collected, washed with PBS, fixed with 2% paraformaldehyde for 4 min at 4 °C and permeabilized with cold 70% ethanol. After washing with PBS and 1% BSA, cells were stained with a mix of 40 μg ml^{-1} propidium iodide and 10 μg ml^{-1} DNAse-free ribonuclease A for 30 min at room temperature. Finally, samples were washed with PBS and 1% BSA, and acquired on the flow cytometer (CytoFLEX, Beckman Coulter). Data were evaluated with CytExpert Software (Beckman Coulter).

2.9. Image acquisition and analysis
Samples were imaged using a confocal microscope (Nikon C2) to obtain z-stacks of the 3D minitissues. Images were analyzed using Fiji software. All analyzed images were pre-processed to subtract the background (rolling ball radius = 50 pixels) and to adjust the contrast and brightness levels. Then, images were converted to a binary format by applying a threshold. Images obtained from samples of different conditions were processed using the same parameters to allow comparisons. At least three ROIs were analyzed for each sample and at least three samples were considered for each condition. Images were quantified in terms of area fraction, cell co-localization and vascular network parameters (i.e. total network length, number of junctions) following previously established protocols [27]. Area fraction was used to evaluate growth of CCs or the expression of specific markers. Regarding analyses of cell co-localization, at least five ROIs (200 $\times$ 200 pixels) for at least three samples were taken in regions with vessels or without vessels; the binary image with EC signal was then overlapped with the binary image containing OBs, OCs or CCs to calculate the percentage of overlapping pixels. The same was done for co-localization of CCs with OCs. This way, we were able to evaluate the co-localization of the two populations by superimposing the fluorescence signal of each cell type. Results were expressed in terms of area fraction of co-localizing (Coloc) or not co-localizing (Not Coloc) cells and normalized to Coloc condition.

2.10. Statistical analysis
Prism Graph Pad software was used to perform unpaired Student's t-test to determine significant differences between conditions. Differences were considered significant for $p < 0.05$ (*), $p < 0.01$ (**), $p < 0.001$ (***) and $p < 0.0001$ (****). Results are presented as mean $\pm$ standard error of the mean. Details about p values and number of replicates are reported in each figure legend.

3. Results

3.1. Development and characterization of engineered bone microenvironments
We previously developed a computational/statistical approach which allowed to customize the geometrical parameters of microvascular networks embedded within bone minitissues based on osteo-differentiated MSCs [27]. Here, we employed the minitissue system (figure 1(A)) to develop actively remodeling bone niches embedding the key components of a bone tissue unit (i.e. OBs, OCs, ECs, bone-resident macrophages) under physiological and pathological conditions (i.e. addition of breast CCs).

Morphological and immunofluorescence analyses on OCs and OBs revealed typical features of cell differentiation. Indeed, OCs were multinucleated and presented a rounded morphology with ruffle borders (figure S1(A) (available online at stacks.iop.org/BF/13/035036/mmedia)). OCs expressed the cell identity

Figure 1. Development and characterization of the tissue models. (A) Drawing of the PMMA support on the glass cover slide, containing the fibrin gel and embedded cells. Scale bar: 2 mm. (B) Experimental conditions. Bm: bone minitissue with ECs, OBs and OCs embedded in fibrin. MBm: metastatic bone minitissue, where CCs were added to Bm. (C) IBm: immuno bone minitissue with ECs, OBs, OCs and macrophages (M0) embedded in fibrin. MIBm: metastatic immuno bone minitissue, where CCs were added to IBm. (D), (E) Immunofluorescence images showing the effects of the addition of CCs into the IBm (red: ECs, white: OBs, light blue: OCs, green: breast CCs). Scale bar = 200 μm. (F) Effect of CC addition on vascular density (values normalized on IBm; $p = 0.0508$; $N = 4$). (G) Co-localization of CCs in the minitissue: CCs resulted co-localized with vessels (values normalized on Coloc; **$p = 0.0037$; $N = 5$). (H), (I) Quantification of released matrix metalloproteinase (MMP)-2 and osteopontin (OPN) during minitissue culture. Increased release of the two molecules indicates an actively remodeling bone-like tissue (MMP2: ***Bm, d2 vs. Bm, d7: $p = 0.0008$; MBm, d2 vs. MBm, d7: $p = 0.0016$; IBm, d2 vs. IBm, d7: $p = 0.001$; MIBm, d2 vs. MIBm, d7: $p = 0.0008$; OPN: *MIBm, d2 vs. MIBm, d7: $p = 0.0011$; $N = 3$).

marker RANK (figure S1(A)) and produced more TRAP compared to undifferentiated OCs or monocytes (figure S1(B)). OBs presented a cobblestone morphology and expressed both collagen type I and non-collagenous proteins, namely OPN and osteocalcin (figure S1(C)).

Differentiated OBs, OCs and ECs were then embedded in a fibrin matrix to develop an engineered bone tissue construct, which we labeled as Bm (figure 1(B)). Based on this minitissue, we then enriched the system with breast CCs to mimic the early-metastatic niche (i.e. Metastatic Bone minitissue, MBm) (figure 1(B)). Starting from a homogeneous distribution of cells with pre-determined concentrations, higher order structures self-assembled to mimic a vascularized bone microenvironment (figures S2(A) and (B)). ECs developed a continuous and interconnected microvascular network, which in Bm was significantly longer (9455 ± 444.1 μm vs. 4041 ± 483.6 μm) and more branched (60.5 ± 30.7 vs. 12.4 ± 4.5 number of junctions) compared to the MBm (figures S2(C) and (D)). This quantification represents a preliminary indication of the effect of CCs on ECs which lead to an abnormal vascular architecture and vascular density [33, 34]. Microvascular networks were surrounded by OBs in both minitissues. More in detail, we found that the majority of OB co-localized with ECs in both minitissues

(100 ± 9.6% co-localized cells vs. 22 ± 1.8% not co-localized cells in Bm, 100 ± 10.2% co-localized cells vs. 37.1 ± 7.8% not co-localized cells in MBm) (figure S2(E)). Moreover, most CCs co-localized with vessels in the MBm (100 ± 19.8% co-localized cells vs. 17.6 ± 5.3% not co-localized cells in MBm) (figure S2(F)), recapitulating their close interaction with the vascular niche as observed *in vivo*, where CCs are in close proximity of ECs and OCs [35]. This finding is consistent with the hypothesis that extravasated CCs that remain close to the endothelium have higher potential to form metastasis [36]. Furthermore, the distribution of CCs in the gel in small clusters resembled the *in vivo* organization in micrometastases found during the establishment of the early metastatic niche after CC extravasation in the target tissue, as reported in previous studies [37–39]. It is interesting to highlight that CCs frequently co-localized with OCs in the MBm (not co-localized cells only represented 25.6 ± 10.4% of co-localized cells, 100 ± 12.7%) (figure S2(G)).

We then included M0 macrophages into the Bm and MBm minitissues, generating the IBm and the MIBm, respectively (figure 1(C)). As for the previously described minitissues, ECs developed vascularized networks which were less dense in the MIBm compared to the IBm (100 ± 12.5% vs. 66.2 ± 6.7%) (figures 1(D)–(F), and supplementary video) and

with reduced interconnections (57.2 ± 34.4 vs. 37.4 ± 22.9 number of junctions) (figure S2(H)). Consistent with this observation, we found an increase of IL-20, an anti-angiogenic marker, in the culture medium of the MIBm (64.3 ± 7.7 pg ml^{-1} vs. 51.6 ± 6.4 pg ml^{-1}) (figure S2(I)) [40]. This result possibly suggests a stage that precedes the angiogenic switch as for MBm [34]. As for the Bm and MBm, the vascular networks were surrounded by OBs (100 ± 10.8% co-localized cells vs. 40.1 ± 11.3% not co-localized cells in IBm, 100 ± 3.9% co-localized cells vs. 29.9 ± 6.5% not co-localized cells in MIBm) (figure S2(J)) and CCs (100 ± 15.4% co-localized cells vs. 28.2 ± 8.8% not co-localized cells in MIBm) (figure 1(G)). Finally, we counted a higher number of OCs co-localized with CCs compared to OCs randomly distributed inside the matrix (100 ± 17.1% co-localized cells vs. 87.8 ± 9.1% not co-localized cells in MIBm) (figure S2(K)), following the same trend observed in the MBm (figure S2(G)). The results of co-localization of CCs with OCs in both metastatic minitissues (i.e. MBm and MIBm) could be related to the induction of the 'vicious cycle' by CCs, which recruit OCs and increase their activity in the bone microenvironment [35, 41].

To evaluate the remodeling of the minitissues, we quantified the release of bone related proteins in the culture medium, which is an indication of tissue maturation. We quantified a significant increase of secreted matrix metalloproteinase-2 (MMP2) in all four minitissues from day 2 to day 7 (e.g. MMP2 release in the MIBm increased from 3809 ± 477.8 pg ml^{-1} (day 2) to 8861 ± 467.7 pg ml^{-1} (day 7)) and a release of OPN in the MIBm that significantly increased from 196 ± 14.5 pg ml^{-1} (day 2) to 337.3 ± 8.7 pg ml^{-1} (day 7) (figures (H) and (I)).

Overall, we generated actively remodeling bone-mimicking microenvironments, where the progressive self-assembly of the different cellular components resulted in the development of vascularized tissues with peculiar co-localization patterns. Vascular networks were surrounded by OBs, which expressed bone proteins contributing to the maturation of the tissue constructs over time. Furthermore, both the formation of micrometastases of CCs adjacent to the vessel wall and the close interaction between CCs and OCs represent hallmarks of the establishment of a bone metastatic tumor microenvironment.
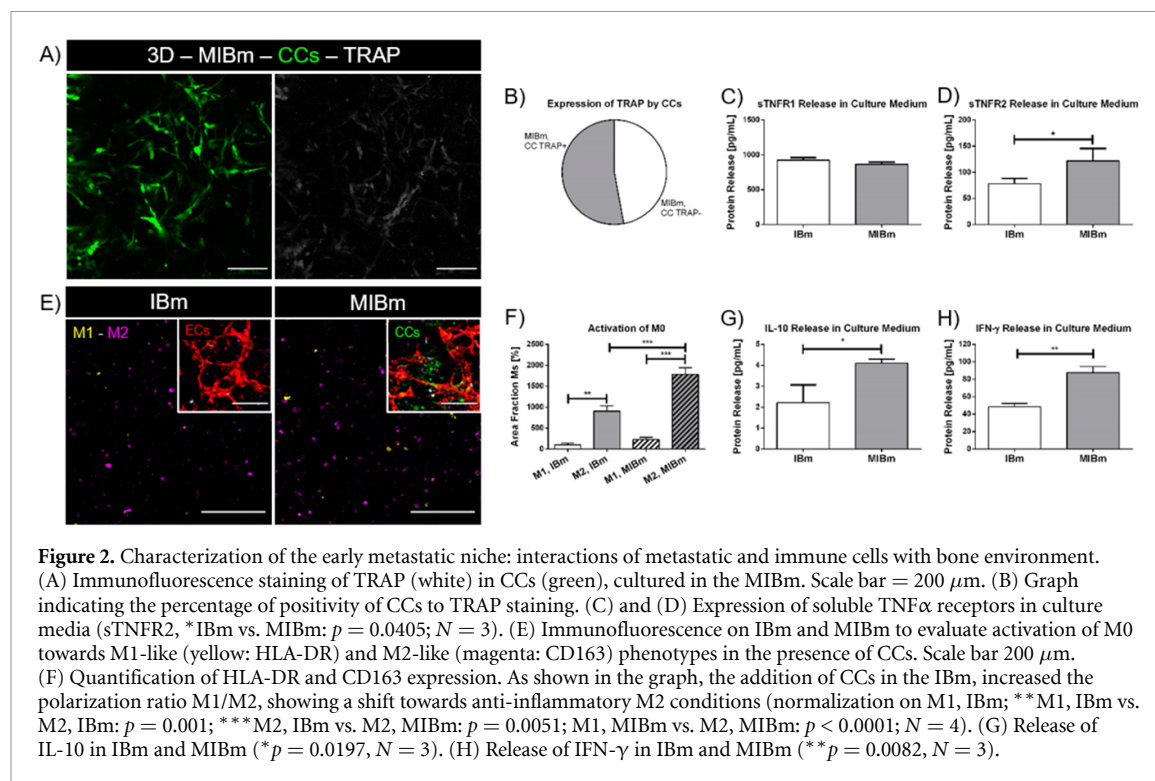
3.2. CCs in bone minitissues acquire osteomimicry properties and modify macrophage activation

After the establishment and characterization of the bone microenvironments, we then focused our attention on the analysis of specific features of the early metastatic niche. First, we evaluated the release of RANKL, which is expressed by OBs and CCs and induces OC activation, and OPG, which inhibits OC differentiation and resorption by sequestering RANKL. Therefore the balance of the RANKL/OPG ratio regulates bone resorption in established osteolytic bone metastases [42]. We observed a significant unbalance of the RANKL/OPG ratio comparing the Bm with the other minitissues (0.79 ± 0.03 in Bm, 0.57 ± 0.03 in MBm, 0.57 ± 0.07 in IBm, 0.52 ± 0.02 in MIBm) (figure S3(A)). RANKL should be highly expressed in the tumor microenvironment, but the RANKL/OPG ratio significantly decreased by adding CCs, M0 macrophages or both due to the higher expression of OPG (41.2 ± 3.4 pg ml^{-1} in Bm, 49.9 ± 4.1 pg ml^{-1} in MBm, 44.2 ± 5.2 pg ml^{-1} in IBm, 62.1 ± 3.0 pg ml^{-1} in MIBm) compared to the Bm (figure S3(B)) [43]. The presence of OPG, in particular in the MIBm, could suggest that CCs and M0 macrophages activated the bone microenvironment to secrete OPG and restore the homeostasis of the tissue [44]. On the other hand, the release of RANKL in the culture medium did not change in the bone minitissues (32.3 ± 1.5 pg ml^{-1} in Bm, 28.4 ± 1.7 pg ml^{-1} in MBm, 24.8 ± 2.3 pg ml^{-1} in IBm, 32.2 ± 2.6 pg ml^{-1} in MIBm) (figure S3(C)). Focusing our attention on the MIBm, we hypothesized that the low detection of RANKL could be explained by CCs sequestering soluble RANKL, since more than 50% of CCs in MIBm expresses TRAP (52.9 ± 9.5%), hence acquiring features of OCs (figures 2(A) and (B)).

TRAP expressing OCs are known to interact with RANKL to start the bone resorption program [45]. Here, CCs and OCs had different morphologies and organization. Indeed, CCs were elongated and clustered together, while OCs were round and maintained a single cell distribution. For this reason, the TRAP signal of the two populations could be clearly discriminated through immunofluorescence. Trying to prove the hypothesis of CCs hijacking RANKL in MIBm, we showed that CCs in presence of RANKL are capable to absorb bone matrix. First, we incubated CCs with RANKL for 14 d following the same protocol that we used for monocyte differentiation into OCs and we noticed a significantly higher expression of TRAP in CCs under RANKL stimulation (100.0 ± 15.1% 2D, Ctrl vs. 316.6 ± 51.1% 2D, +RANKL) (figures S3(E) and (D)). Then, we cultured CCs on dentine slices for 14 d and we observed a higher number of bone resorption pits in presence of CCs treated with RANKL (100.0 ± 22.6% −RANKL vs. 277.5 ± 78.4% +RANKL), suggesting an induced osteolytic activity of CCs (figures S3(F) and (G)) [46]. Overall, TRAP expression and bone resorption indirectly showed the ability of CCs to mimic features of OCs in MIBm (i.e. osteomimicry).

We then analyzed the release of soluble receptors (soluble tumor necrosis factor receptor, sTNFR1 and sTNFR2) derived from a proteolytic processing by the metalloproteinase TNF-α-converting enzyme (TACE) that are important for the limitation of

Figure 2. Characterization of the early metastatic niche: interactions of metastatic and immune cells with bone environment. (A) Immunofluorescence staining of TRAP (white) in CCs (green), cultured in the MIBm. Scale bar = 200 μm. (B) Graph indicating the percentage of positivity of CCs to TRAP staining. (C) and (D) Expression of soluble TNFα receptors in culture media (sTNFR2, *IBm vs. MIBm: $p = 0.0405$; $N = 3$). (E) Immunofluorescence on IBm and MIBm to evaluate activation of M0 towards M1-like (yellow: HLA-DR) and M2-like (magenta: CD163) phenotypes in the presence of CCs. Scale bar 200 μm. (F) Quantification of HLA-DR and CD163 expression. As shown in the graph, the addition of CCs in the IBm, increased the polarization ratio M1/M2, showing a shift towards anti-inflammatory M2 conditions (normalization on M1, IBm; **M1, IBm vs. M2, IBm: $p = 0.001$; ***M2, IBm vs. M2, MIBm: $p = 0.0051$; M1, MIBm vs. M2, MIBm: $p < 0.0001$; $N = 4$). (G) Release of IL-10 in IBm and MIBm (*$p = 0.0197$, $N = 3$). (H) Release of IFN-γ in IBm and MIBm (**$p = 0.0082$, $N = 3$).
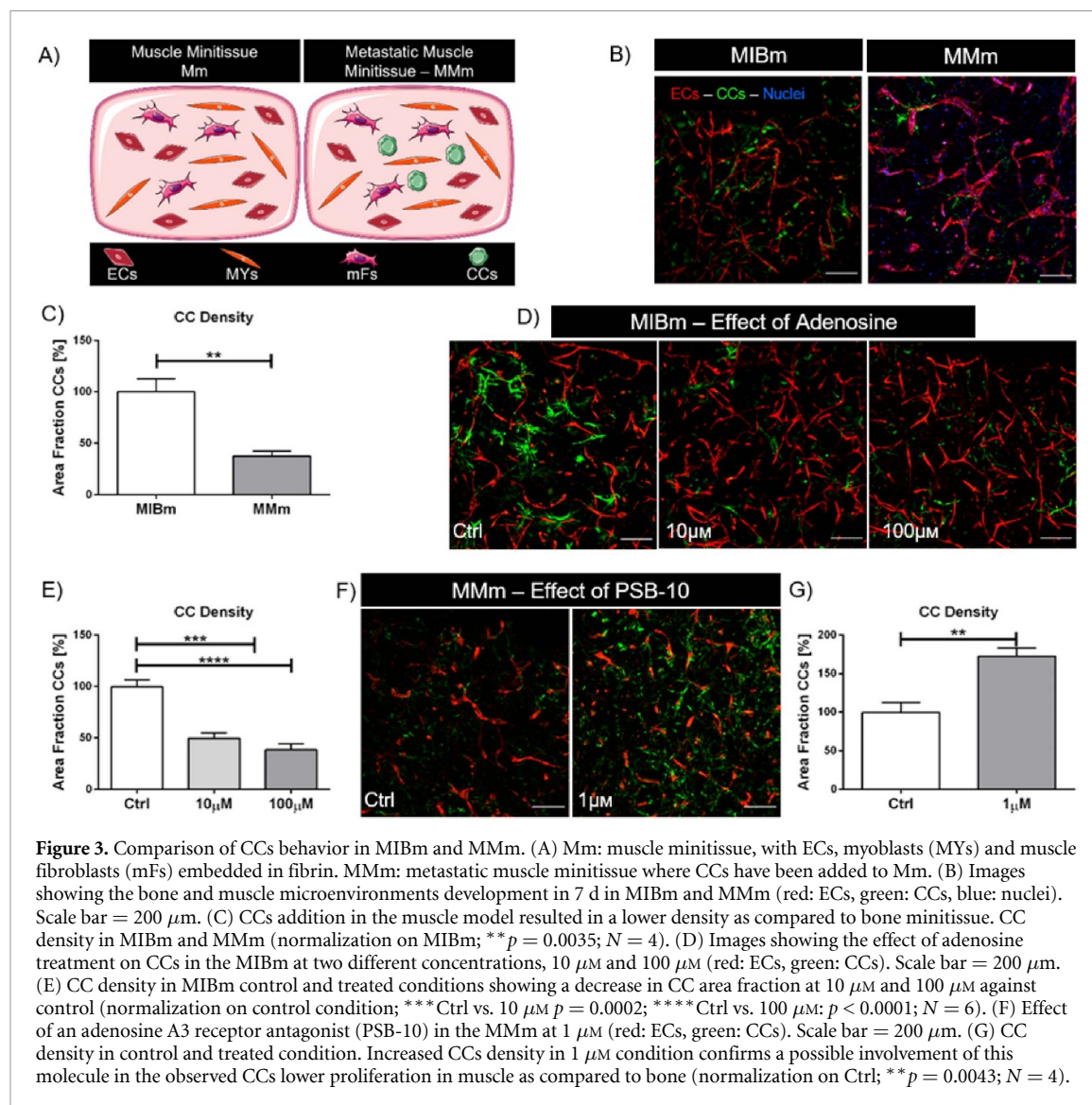
the inflammatory response and are associated to patient's survival with bone metastasis [47]. CCs induced a decrease in the release of these soluble receptors, which was significant for sTNFR1 (e.g. sTNFR1: 924.4 $\pm$ 21.2 pg ml^{-1} in IBm and 865.5 $\pm$ 18.1 pg ml^{-1} and MIBm; sTNFR2: 121.9 $\pm$ 13.5 pg ml^{-1} in IBm and 98.0 $\pm$ 2.6 pg ml^{-1} in MIBm) (figures 2(C) and (D)). The decrease of both soluble receptors in presence of CCs is particularly relevant because sTNFR act as inhibitors of TNF by sequestering it [48]. Hence, CCs seem to modulate the bone microenvironment to promote the growth of a metastatic lesion. Finally, we observed that the processed form of the TNF-related 'a proliferation-inducing ligand' (APRIL, 17 kDa) released into the culture medium, which is an indication of metastatic invasion, was significantly higher in the MIBm (87.6 $\pm$ 7.0 pg ml^{-1}) compared to the IBm (48.4 $\pm$ 3.9 pg ml^{-1}) (figure S3(H)) [49, 50].

After the analysis of the effect of CCs in the early bone metastatic niche, we focused on the activation of M0 macrophages in the IBm and MIBm. We acknowledge that the nomenclature for macrophage activation is still under debate, so in this work we used the traditional classification proposed by Mills who distinguished between 'classically activated' inflammatory M1 macrophages and 'alternatively activated' anti-inflammatory M2 macrophages and we tried to identify the stimulus that led to M0 activation [51, 52]. We performed immunofluorescence analyses on IBm and MIBm for the M1-like marker HLA-DR and for the M2-like marker CD163, and we analyzed the release of proteins related to

M0 macrophage activation [53]. More in detail, immunofluorescence revealed a significant expression of CD163 in both minitissues in terms of area fraction with respect to HLA-DR (100 $\pm$ 40.8% in M1, IBm, 905.7 $\pm$ 128.8% in M2, IBm, 226.8 $\pm$ 52.1% in M1, MIBm and 1784 $\pm$ 158.4% in MIBm) (figures 2(E) and (F)). The expression of CD163 was significantly different between the two minitissues. The increase in expression of M2-like marker in the MIBm could be partially explained with the significant increase of IL-10 release in the microenvironment (2.2 $\pm$ 0.5 pg ml^{-1} vs. 4.1 $\pm$ 0.1 pg ml^{-1}) (figure 2(G)). Indeed, the presence of IL-10 could lead to the activation of M0 macrophages towards an M2-like phenotype [52]. Moreover, this activation recapitulates the phenotype of TAMs that are strictly linked to the development of the metastatic process [54]. On the other hand, the expression of HLA-DR slightly increased between IBm and MIBm (figure 2(F)). This rise could be due to the significant increase of IFN-γ released in the MIBm compared to the IBm (87.6 $\pm$ 7.0 pg ml^{-1} vs. 48.4 $\pm$ 3.9 pg ml^{-1}) (figure 2(H)). Indeed IFN-γ is related to the activation of M1-like macrophages [55]. These results are supported by immunofluorescence for the same markers HLA-DR and CD163 that were performed on M0 macrophages seeded in 2D with or without CCs (figure S3(I)), where we quantified a significant increase in the presence of CD163 positive macrophages in both conditions (100 $\pm$ 15% for M1-like macrophages in monoculture vs. 589.2 $\pm$ 65.4% for M2-like macrophages in monoculture vs. 144.7 $\pm$ 33.0% for M1-like

Figure 3. Comparison of CCs behavior in MIBm and MMm. (A) Mm: muscle minitissue, with ECs, myoblasts (MYs) and muscle fibroblasts (mFs) embedded in fibrin. MMm: metastatic muscle minitissue where CCs have been added to Mm. (B) Images showing the bone and muscle microenvironments development in 7 d in MIBm and MMm (red: ECs, green: CCs, blue: nuclei). Scale bar = 200 μm. (C) CCs addition in the muscle model resulted in a lower density as compared to bone minitissue. CC density in MIBm and MMm (normalization on MIBm; $**p = 0.0035$; $N = 4$). (D) Images showing the effect of adenosine treatment on CCs in the MIBm at two different concentrations, 10 μM and 100 μM (red: ECs, green: CCs). Scale bar = 200 μm. (E) CC density in MIBm control and treated conditions showing a decrease in CC area fraction at 10 μM and 100 μM against control (normalization on control condition; $***$Ctrl vs. 10 μM $p = 0.0002$; $****$Ctrl vs. 100 μM: $p < 0.0001$; $N = 6$). (F) Effect of an adenosine A3 receptor antagonist (PSB-10) in the MMm at 1 μM (red: ECs, green: CCs). Scale bar = 200 μm. (G) CC density in control and treated condition. Increased CCs density in 1 μM condition confirms a possible involvement of this molecule in the observed CCs lower proliferation in muscle as compared to bone (normalization on Ctrl; $**p = 0.0043$; $N = 4$).

macrophages in co-culture vs. $479.9 \pm 69.5\%$ for M2-like macrophages in co-culture) (figure S3(J)).

Overall, we demonstrated that the engineered minitissues show typical features of a metastatic bone microenvironment including the expression of key bone remodeling markers and the polarization of macrophages. These parameters could be used to monitor the dynamic response of the system to anti-metastatic therapies. Hereinafter, we will use the MIBm for further analyses, since the addition of the immune component could better mimic the *in vivo* early bone metastatic niche.

3.3. A muscle-like microenvironment reduces the growth of CCs as compared to bone through adenosine production

The bone tissue is a primary target for breast CC invasion and it is reported that about 70% advanced breast cancer patients develop bone metastases [2]. Surprisingly, the skeletal muscle is not a specific target organ of breast cancer. Therefore, the muscle microenvironment represents an appropriate soil to verify the

organ-tropism of breast CCs towards bone. We initially developed a Muscle minitissue (Mm) based on the co-culture of ECs, myoblasts (MYs) and mFs in a fibrin matrix (figure 3(A)).

The addition of breast CCs allowed us to generate a MMm (figure 3(A)), which we then compared to the bone minitissue (figure 3(B)). It is important to highlight that the purpose of these muscle minitissues is not to fully recapitulate the architecture of the muscle tissue (e.g. myofiber and collagen matrix alignment), but to quantify the effect of the muscle cellular components on breast CCs. Here, both muscle minitissues included organ-specific fibroblasts, since it is rapidly emerging how fibroblasts from different tissues have specific transcriptional profiles and functionalities [56]. For this reason, we evaluated the behavior of muscle-specific and lung-specific fibroblasts by measuring the proliferation of breast CCs on 2D cultures. Muscle (mFs) or lung (lFs) fibroblasts were seeded with CCs at a 1:1 density ratio. The proliferation of breast CCs was significantly lower when co-cultured with mFs ($55.2 \pm 4.5\%$) compared to lFs ($90 \pm 8.6\%$)

or CC monocultures (101 ± 8.3%) (figure S4(A)). This result suggests that mFs might be critical determinants of the anti-metastatic properties of the skeletal muscle and provides a strong rationale for their inclusion into the MMm. Indeed, the effect of mFs on breast CCs is very different from the one of tumor associated fibroblasts that emerged in other tumor target tissues [57].

ECs were able to develop vascular structures in both Mm and MMm (figures S4(B) and (C)), although less interconnected compared to the vasculature generated in the bone minitissues (figures S4(D) and S2(H)). As previously observed for the bone-mimicking tissue constructs, breast CCs preferentially co-localized with ECs in the MMm (figure S4(E)), suggesting that this behavior could mimic the *in vivo* perivascular niche as a hospitable microenvironment for dormant tumor cells both in non-specific and specific target tissues [58]. On the other hand, MYs and mFs remained homogeneously distributed in the matrix.

We then compared the two microenvironments observing that the proliferation of breast CCs was significantly lower in the MMm (100.0 ± 12.6% vs. 37.7 ± 4.5%), as showed by the analysis of the area fraction covered by CCs (figures 3(B) and (C)). Overall, our minitissues reproduced the typical organ-specific growth of breast CCs into the bone microenvironment, as observed *in vivo* [59].

Looking for potential molecular mechanisms explaining the decreased presence of breast CCs into the skeletal muscle, we previously found that adenosine might play a critical role [60]. In addition, adenosine treatment was shown to reduce the burden of breast cancer bone metastases in mice [61]. We then sought to determine if the addition of adenosine at different concentrations to the culture medium of the bone minitissue could reduce the growth of breast CCs. We treated the constructs with physiological levels of adenosine (10 μM and 100 μM), finding that the proliferation of breast CCs was significantly impaired in both conditions (100 ± 6.7% at Ctrl, 49.6 ± 5.4% at 10 μM and 38.6 ± 5.9% at 100 μM) (figures 3(D) and (E)). It is important to highlight that the development of vascular networks was not affected by both adenosine concentrations (figure 3(D)), suggesting that no major side effects were induced by the compound. To show that muscle-secreted adenosine was actually responsible for the limited formation of breast cancer metastases into skeletal muscle, we then treated the MMm with an antagonist of the A$_3$ adenosine receptor (i.e. PSB-10). This compound was previously shown to increase the extravasation of breast CCs in a microfluidic skeletal muscle model by altering the adenosine-mediated cross-talk between muscle and CCs [60]. The MMm was incubated with 1 μM PSB-10 and the system was kept in culture for 7 d. Breast CC proliferation increased in presence of PSB-10 (100.0 ± 12.7%

vs. 172.8 ± 10.3%) (figures 3(F) and (G)). Furthermore, the formation of interconnected vascular networks was partially compromised compared to control MMm (figure 3(F)). However, we did not quantify obvious differences in terms of vessel formation comparing Mm and MMm (no PSB-10 addition, figure S4(B)). Hence, it is possible that the addition of PSB-10 limited the development of vascular structures or that the same effect was due to the over-proliferation of breast CCs.

Together, the increase in breast CC growth with PSB-10 indirectly confirms the presence of adenosine in the MMm, as well as the protective role of this molecule against breast cancer metastases in the muscle microenvironment.

3.4. The MIBm as a tool to study the effects of anti-metastatic therapies

Chemotherapy is still one of the major therapeutics for the treatment of breast cancer, including the use of anthracyclines like DOX and inhibitors of the mTOR (mammalian target of rapamycin) pathway [62, 63]. Even if those compounds have anti-tumoral properties, they have significant toxicity for the microenvironment, in particular on the vascular compartment [64, 65]. For these reasons, we decided to test DOX and rapamycin in the MIBm to evaluate the reactivity of the bone microenvironment to anti-metastatic drugs. More in detail, we investigated the effect of DOX and rapamycin on the MIBm and compared the results with a simplified cancer control minitissue (CCm), embedding only CCs in a fibrin gel. Indeed, the complex MIBm allows to quantify the effect of a specific drug on both the tumoral and vascular components of the system and to evaluate the contribution of the microenvironment on the drug sensitivity of CCs.

We first analyzed the effect of DOX on the MIBm and CCm. The growth and arrangement of breast CCs were different in the two minitissues, in both control and DOX-treated conditions (figure 4(A)).

Indeed, breast CCs in the MIBm showed low proliferation and preferentially aggregated in clusters surrounding the vessels, while in the simplified CCm the same cells showed higher proliferation and a single cell distribution with a rounded morphology. In treated condition, the growth of breast CCs was significantly reduced in presence of 1 μM DOX due to the anti-proliferative effect of this drug (figure 4(B)). However, the effect of DOX was much more limited in the complex MIB, with a significant 2.24-fold reduction of CC growth compared to 16.7-fold reduction in simplified CCm. These results highlight the relevance of minitissues, which closely mimic the early metastatic niche, for an effective drug testing compared to more simplistic models or traditional 2D cultures that lack a tissue-like microenvironment which interferes with CC behavior and drug efficacy [66]. The main effect of DOX on CCs is to arrest the cell cycle in the
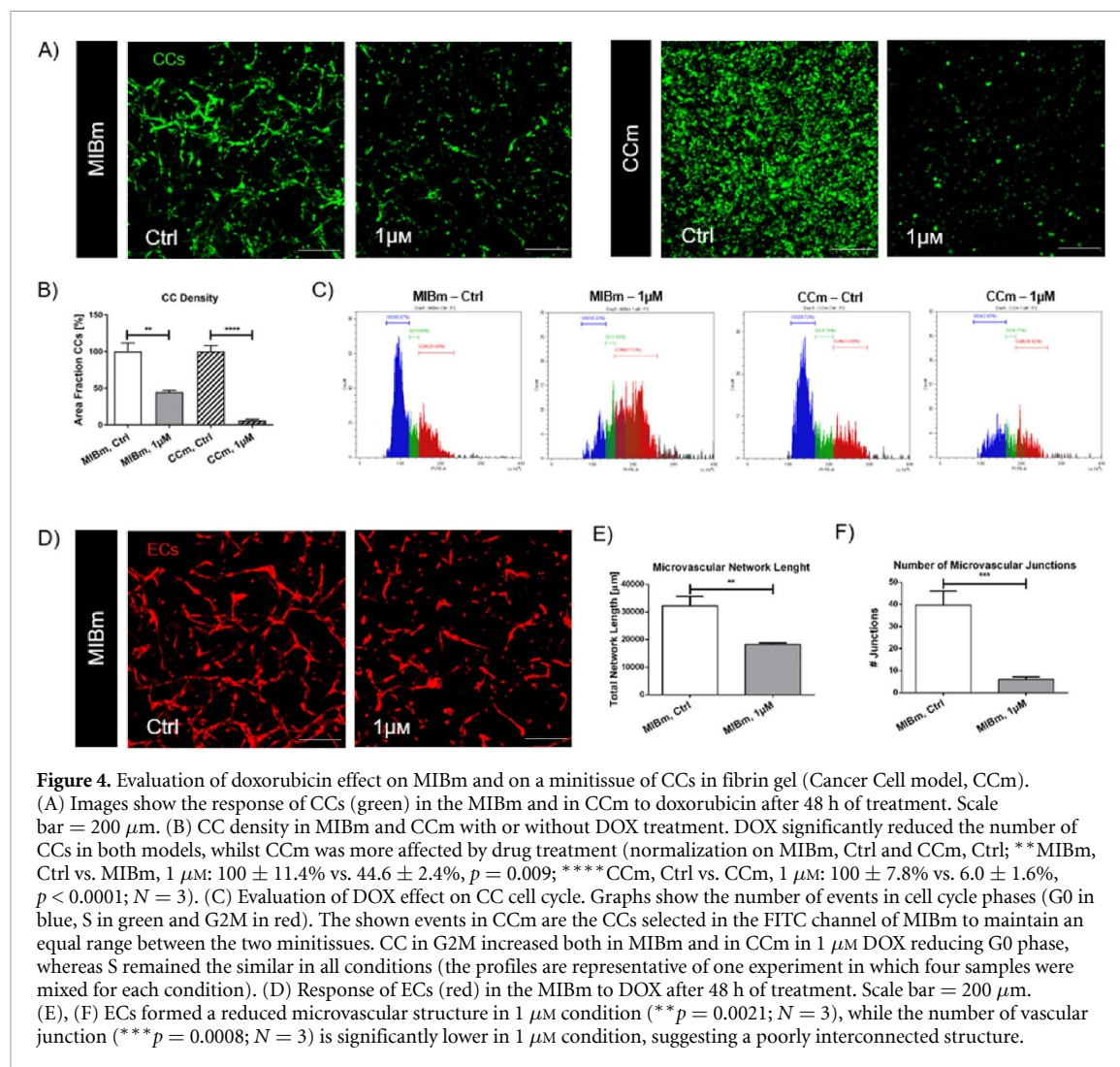
Figure 4. Evaluation of doxorubicin effect on MIBm and on a minitissue of CCs in fibrin gel (Cancer Cell model, CCm).
(A) Images show the response of CCs (green) in the MIBm and in CCm to doxorubicin after 48 h of treatment. Scale
bar = 200 μm. (B) CC density in MIBm and CCm with or without DOX treatment. DOX significantly reduced the number of
CCs in both models, whilst CCm was more affected by drug treatment (normalization on MIBm, Ctrl and CCm, Ctrl; **MIBm,
Ctrl vs. MIBm, 1 μM: 100 ± 11.4% vs. 44.6 ± 2.4%, $p = 0.009$; ****CCm, Ctrl vs. CCm, 1 μM: 100 ± 7.8% vs. 6.0 ± 1.6%,
$p < 0.0001$; $N = 3$). (C) Evaluation of DOX effect on CC cell cycle. Graphs show the number of events in cell cycle phases (G0 in
blue, S in green and G2M in red). The shown events in CCm are the CCs selected in the FITC channel of MIBm to maintain an
equal range between the two minitissues. CC in G2M increased both in MIBm and in CCm in 1 μM DOX reducing G0 phase,
whereas S remained the similar in all conditions (the profiles are representative of one experiment in which four samples were
mixed for each condition). (D) Response of ECs (red) in the MIBm to DOX after 48 h of treatment. Scale bar = 200 μm.
(E), (F) ECs formed a reduced microvascular structure in 1 μM condition (**$p = 0.0021$; $N = 3$), while the number of vascular
junction (***$p = 0.0008$; $N = 3$) is significantly lower in 1 μM condition, suggesting a poorly interconnected structure.

G2M phase, hence reducing their proliferation [67].
According to these findings, we observed an increase
in the percentage of CCs in G2M phase in both min-
itissues (Ctrl: 28.5% in MIBm and 23.7% in CCm;
1 μM DOX: 67.1% in MIBm and 38.9% in CCm)
with a 1.43-fold higher percentage in MIBm respect
to CCm (figure 4(C)). It is interesting to highlight
that in both minitissues and conditions the number
of events in the S phase remained similar (the dif-
ference of mean of events in S phase between con-
trol and 1 μM DOX is 0.6 ± 2.5%). We also evaluated
the side effects of DOX on the microenvironment of
the MIBm, mainly focusing on ECs (figure 4(D)). The
length of microvascular networks (32 228 ± 1956 μm
vs. 18 201 ± 338.1 μm) and the number of junctions
(39.7 ± 3.7 vs. 6.0 ± 0.6) were reduced in presence
of 1 μM DOX, indicating less developed and intercon-
nected vascular structures (figures 4(E) and (F)) and
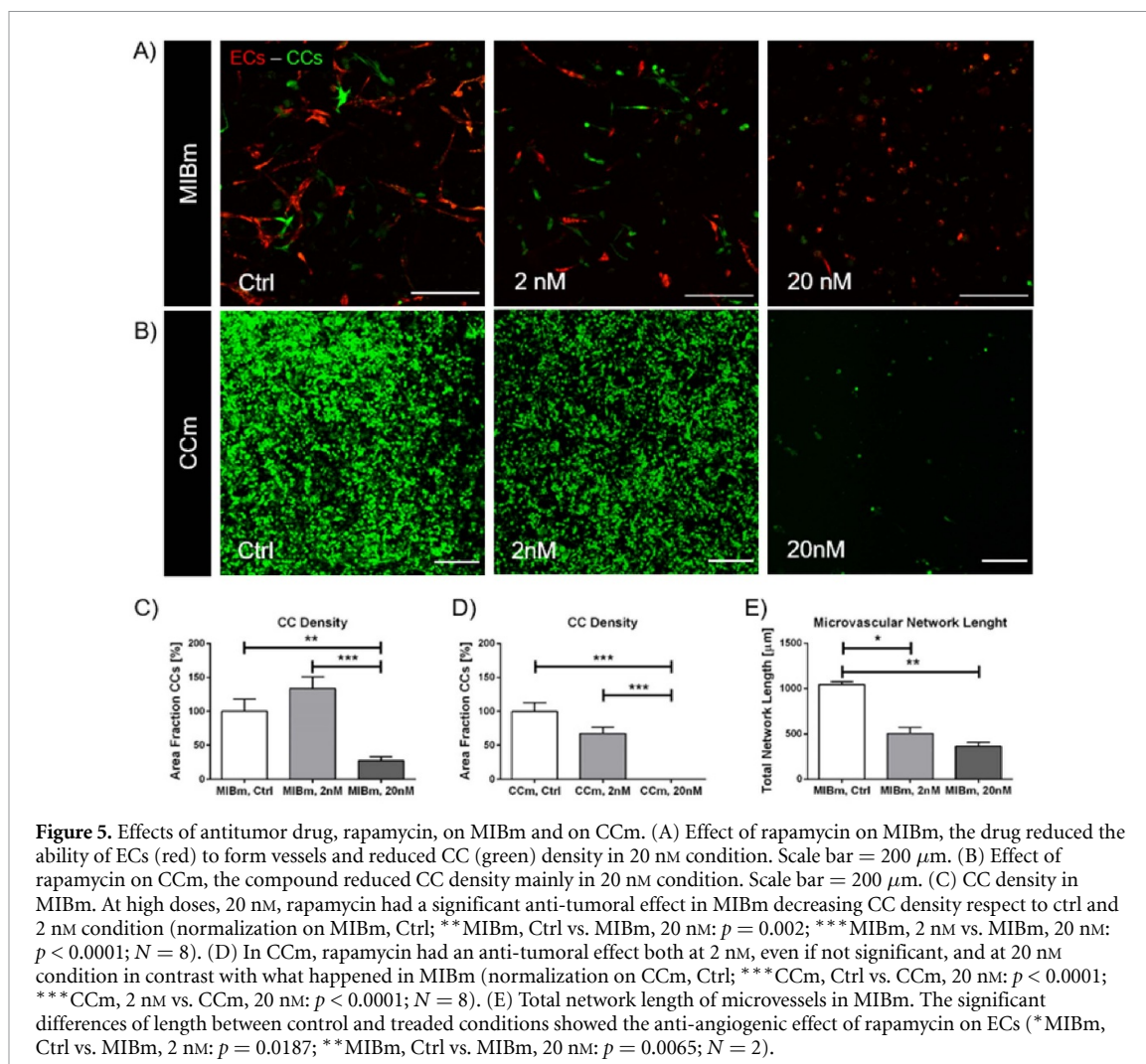reflecting the toxicity of DOX for ECs [68].

As a second test, we treated both the MIBm and
CCm with rapamycin (figures 5(A) and (B)).

Low concentration of rapamycin (i.e. 2 nM) did
not determine any reduction in breast CC coverage

in the MIBm (100 ± 18.4% Ctrl vs. 133.6 ± 17.2%
in 2 nM vs. 27.3 ± 5.8% in 20 nM) (figure 5(C))
while inducing a decrease in the area covered by the
same cells in the simplified CCm (100 ± 12.7% Ctrl
vs. 67.2 ± 9.8% in 2 nM vs. 0.2 ± 0.1% in 20 nM)
(figure 5(D)). Increasing the drug concentration to
20 nM we did observe a significant decrease in breast
CC area fraction, although less pronounced in the
MIBm. The effect of rapamycin was also confirmed
by immunofluorescence for the proliferation marker
Ki67 (figures S5(A) and (B)), showing a significant
dose dependent decrease of Ki67 expression and an
increase of quiescent cells. Finally, treatment with
rapamycin significantly reduced the length of the vas-
cular structures in the MIBm from 1045 ± 29.9 μm
in controls to 504.4 ± 68.7 μm in 2 nM and to
360.6 ± 46.9 μm in 20 nM (figure 5(E)), in agreement
with the anti-angiogenic properties of the drug [69].

Overall, we showed that the MIBm responded to
two FDA approved anti-cancer drugs. Most import-
antly, we pointed out that the complexity of the bone
microenvironment plays a critical role in mediating
the anti-metastatic effects of these compounds.

Figure 5. Effects of antitumor drug, rapamycin, on MIBm and on CCm. (A) Effect of rapamycin on MIBm, the drug reduced the ability of ECs (red) to form vessels and reduced CC (green) density in 20 nM condition. Scale bar = 200 μm. (B) Effect of rapamycin on CCm, the compound reduced CC density mainly in 20 nM condition. Scale bar = 200 μm. (C) CC density in MIBm. At high doses, 20 nM, rapamycin had a significant anti-tumoral effect in MIBm decreasing CC density respect to ctrl and 2 nM condition (normalization on MIBm, Ctrl; **MIBm, Ctrl vs. MIBm, 20 nM: $p = 0.002$; ***MIBm, 2 nM vs. MIBm, 20 nM: $p < 0.0001$; $N = 8$). (D) In CCm, rapamycin had an anti-tumoral effect both at 2 nM, even if not significant, and at 20 nM condition in contrast with what happened in MIBm (normalization on CCm, Ctrl; ***CCm, Ctrl vs. CCm, 20 nM: $p < 0.0001$; ***CCm, 2 nM vs. CCm, 20 nM: $p < 0.0001$; $N = 8$). (E) Total network length of microvessels in MIBm. The significant differences of length between control and treaded conditions showed the anti-angiogenic effect of rapamycin on ECs (*MIBm, Ctrl vs. MIBm, 2 nM: $p = 0.0187$; **MIBm, Ctrl vs. MIBm, 20 nM: $p = 0.0065$; $N = 2$).

4. Discussion

We developed 3D human vascularized bone minitissues able to mimic some features of the early-metastatic niche (e.g. CC micrometastases, CC proximity to ECs and OCs, M0 macrophage activation), which could be used as a system to investigate the establishment and progression of breast cancer metastases and to evaluate the response to anti-tumor drugs. Specifically, we implemented a new 3D mini-tissue by embedding fully differentiated human OBs, OCs, ECs, M0 macrophages and CCs in a matrix of fibrin gel. Through this system, we analyzed the mutual interactions of cells occurring in such a complex bone-like microenvironment. We observed the organ-tropism of breast CCs towards bone by comparison with a simplified muscle minitissue. Finally, we showed the different effects of two FDA approved drugs for the treatment of breast cancer (i.e. doxorubicin and rapamycin) on the complex bone minitissue compared to a simpler 3D culture of CCs and we demonstrated how recapitulating the cellular complexity of the bone metastatic microenvironment is essential to truly evaluate the effects of anti-metastatic treatments.

Recent literature highlighted the importance of designing new models for testing anti-metastatic compounds, leveraging on the different efficacy of drugs tested in 2D vs. 3D vs. animal models or mono-culture vs. co-culture systems [70]. However, only a few studies reported the combined use of more than two cell types to develop a 3D co-culture system of osteolytic bone metastasis, including works by Krishnan *et al* and Villasante *et al*, although in the context of Ewing Sarcoma [71–73]. A different approach was adopted by Salamanna *et al*, who employed an ex vivo human bone model to analyze differences characterizing breast and prostate cancer metastases in a dynamic culture system [74]. These strategies allowed to characterize the global effect of different metastatic CCs on the bone homeostasis. However, they did not allow to monitor the behavior of single cell populations and to analyze their interactions with the microenvironment. Recently, Quent *et al* proposed a tissue engineered bone construct with the aim to generate an ectopic humanized bone in mice and to mimic the colonization of breast CCs [75]. Although the authors described the generation of bone constructs with relevant mechanical properties and observed OC recruitment

recapitulating the osteolytic metastasis, the model required long-term maturation and presented features of the host, as construct vascularization by murine cells.

To overcome these limitations, here we developed a minitissue which includes all the major cellular components of the human early metastatic bone microenvironment (i.e. OBs, OCs, ECs, macrophages, CCs), with the final goal to recapitulate the complexity underlying metastatic bone remodeling. Based on previous studies by our group, we embedded differentiated human OBs at high concentration to foster the formation of a mature bone microenvironment and compensate for the initial absence of bone-specific proteins in the original matrix [20, 27]. Though recognizing that we did not recapitulate important structural features of the bone microenvironment, our focus was analyzing how complex cell–cell interactions could drive the expression of key bone metastatic markers and drive the response to anti-metastatic drugs. The concentration of CCs was maintained equal to the one of OCs and M0 macrophages due to their high proliferative potential. This concentration was selected based on preliminary results not reported in this work and consistent with other literature studies [76, 77].

At the cellular level, breast CCs altered the architecture of the vascular system generating disorganized networks that lose the integrity and the hierarchical organization typical of healthy tissues. Consistently with this observation, we found a decrease of total network length in presence of CCs and a reduction of vascular junctions in both metastatic minitissues. While we cannot exclude that the presence of breast CCs simply introduces steric hindrance and impairs vessel growth, it is possible that this phenomenon is a sign of the non-angiogenic stage preceding the angiogenic switch of metastases that finally leads to abnormal vascular geometrical structures [33, 34]. This interpretation is supported by the increased release of IL-20 in presence of CCs that is known to impair vessel growth [40].

Disseminating CCs extravasate in target tissues and enter in a dormancy stage remaining close to the vessels. Indeed, the endothelial niche is an important player in regulating the activation of dormancy programs [36, 78]. In the present study we observed that CCs mainly co-localized with ECs, supporting the idea that their crosstalk is critical to promote the metastatic progression. Moreover, in MIBm CC organization in micrometastases and co-localization with ECs and OCs are peculiar aspects of bone metastasis formation observed *in vivo* [35, 38].

At the molecular level, breast CCs shift the expression of bone-specific proteins by OBs (e.g. MMP2 and OPN) and induce phenotypic changes on bone-resident macrophages, generating an environment which promotes tumor growth and immune evasion [79–81]. Here, we recapitulated typical features of

these processes, including the appearance of a few M1-like macrophages in a population of M2-like macrophages and the unbalanced expression of key proteins that reflects the initial steps of bone metastatic formation (e.g. sTNFRs, IL-10, APRIL). The appearance of the M2-like phenotype was induced by the presence of IL-10 and resembled the TAM properties [52]. TAMs are known to have pro-tumor function and collaborate with bone cells in the release of pro-angiogenic factors and matrix-degrading enzymes, fostering the metastatic process [82, 83]. It is also important to highlight the contribution of the bone microenvironment in M0 macrophages activation. Indeed, in 2D co-culture of M0 macrophages and CCs we evaluated that the majority of M0 macrophages were activated towards a M2-like phenotype, but in a lower quantity respect to M0 macrophages monoculture, differently from what happened in 3D. Highlighting once again the importance of the bone microenvironment in mimicking the breast cancer metastasis. Breast CCs also increase the bone resorption activity of OCs, promoting the formation of osteoporotic bones [41]. In this context, a peculiar aspect of breast CCs is their ability to acquire OC-like properties (i.e. osteomimicry), as observed *in vivo* by their ability to express TRAP [46, 84]. Here, we observed that CCs stimulated with RANKL expressed the OC marker TRAP and were able to generate pits into dentine slides. This observation is consistent with the expression of TRAP by CCs in the MIBm, suggesting that a complex microenvironment producing multiple factors (e.g. RANKL) is responsible for the phenotypic switch of CCs. The hijacking of RANKL by CCs could explain the decrease of soluble RANKL in the MIBm, leading to a decrease of the RANKL/OPG ratio. On the other hand, we also detected an increase of OPG in the MIBm, which is in agreement with the anti-metastatic role of OPG during the initial phases of metastases [44]. We need to highlight that over time the RANKL/OPG ratio increases in bone metastases determining the establishment of the 'vicious cycle'. Here, we limited our analysis to the initial steps of bone metastases and we could only observe some features of the metastatic cascade [2].

As previously mentioned, breast CCs rarely metastasize to the skeletal muscle. Indeed, *in vivo* studies reported no CC invasion in muscle tissues in tumor cell-injected mice [28]. Hence, a muscle minitissue was implemented to assess the organ-tropism of breast CCs to the MBms. This comparison could be instrumental for the discovery of mechanisms that decrease the formation of breast cancer metastases [28]. The muscle minitissue embedded multiple cell types typical of the muscle microenvironment (i.e. MYs, mFs, ECs), being aware that we were not replicating the architecture of the muscle tissue as in our previous work [85]. Rather, we focused on the study of the effects that the muscle tissue cellular

composition had on metastatic cells. CCs co-localized with ECs as in the MIBm, but we quantified a significant decrease of breast CC growth compared to the bone microenvironment, replicating the organ-specific growth of breast CCs observed *in vivo* [86]. mFs could be involved in counteracting CC growth, but other factors could also be responsible for the reduced invasion of breast CCs in muscle [57]. For instance, muscle-secreted adenosine might represent a promising molecule preventing muscle colonization by breast CCs [87]. We observed impaired breast CC growth in the MIBm in presence of adenosine without major side effects on the other cells (i.e. ECs), in accordance with our previous findings [60]. As a control, we treated the MMm with PSB-10, an antagonist of the A_3 adenosine receptor that was shown to increase the extravasation of CCs in a muscle minitissue [60]. We quantified an increase of CC density and partial impairment of vascularization, possibly due to a side effect of PSB-10 and in agreement with the above-mentioned work [60]. Overall, these results suggest the potential use of adenosine as anti-metastatic compound due to its protective role in the skeletal muscle tissue and demonstrate that the MIBm could be used to test anti-tumoral compounds.

We then evaluated the reactivity of our minitissue to two anti-tumoral compounds (i.e. doxorubicin and rapamycin) to assess the possibility of applying the MIBm for drug screening. We tested the drugs both on the MIBm and on a 3D minitissue containing only CCs (i.e. CCm). Interestingly, CCs had a different proliferation rate (i.e. higher in the CCm) and acquired a different morphology in the two minitissues (i.e. clustered and co-localized with ECs in the MIBm, single-cell in the CCm). Those different patterns probably played an important role on drug efficacy, leading to a more marked effect of DOX and rapamycin in CCm. We analyzed the G2M cell cycle arrest of CCs to verify the efficacy of DOX in our minitissues, as shown in literature [67]. This effect led to CC reduced proliferation, which was higher in CCm than in MIBm. Similarly, a significant effect of rapamycin on MIBm was possible only by increasing the concentration of the drug, as shown also by the increase of quiescent CCs (i.e. decrease of Ki67 expression). The dose dependent trend of the drug could resemble the difference between *in vitro* and *in vivo* drug testing. Indeed, the administered dose in animal testing is generally higher compared to *in vitro* cultures [68]. Our results suggest that drug performance is impaired by increasing the complexity of the treated system and on the interaction of tumor cells with the bone microenvironment [88]. In this context, the use of 3D advanced models, as our bone metastatic minitissue, could be useful to better predict the outcome of drug screening in animal models.

Finally, we investigated the side effect of the drugs on other cellular components, in particular their anti-angiogenic properties. Here, DOX and rapamycin impaired the quality of the vascular network, reducing the number of vascular junctions under DOX treatment and the total network length in both drug tests, in accordance with other studies [68, 69].

Concluding, we analyzed the response of the minitissue to compounds with different mechanisms of action including adenosine, rapamycin and doxorubicin showing that the effect of the drug was strictly dependent on the presence of the multicellular bone microenvironment, as demonstrated by immunofluorescence and cytofluorimetry. At the same time, we were able to quantify the effects of the drugs on other often neglected components of the bone microenvironment, including microvascular networks.

5. Conclusions

To our knowledge, we designed one of the most complete cellular models of early bone metastases which we employed to analyze features of metastatic bone including M0 macrophage activation, CCs osteomimicry and co-localization with ECs and OCs. The generation of this heterogeneous cellular microenvironment was shown to play a fundamental role in mediating the response to approved anti-metastatic drugs, suggesting that recreating the *in vivo* complexity is the key to better understand neglected mechanisms of action of already approved drugs, to better predict *in vivo* outcomes and to discover novel potential therapeutic targets.

Data availability statement

The data that support the findings of this study are available upon reasonable request from the authors.

Acknowledgments

ORCID iDs

Maria Vittoria Colombo ⬡ https://orcid.org/0000-0002-6018-9920
Simone Bersini ⬡ https://orcid.org/0000-0003-4620-3500
Chiara Arrigoni ⬡ https://orcid.org/0000-0001-6808-1642
Gabriele Candiani ⬡ https://orcid.org/0000-0003-0575-068X
Giovanni Lombardi ⬡ https://orcid.org/0000-0002-8365-985X
Matteo Moretti ⬡ https://orcid.org/0000-0002-7301-1208

References

[1] Langley R R and Fidler I J 2011 The seed and soil hypothesis revisited-the role of tumor-stroma interactions in metastasis to different organs *Int. J. Cancer* **128** 2527–35

[2] Weilbaecher K N, Guise T A and McCauley L K 2011 Cancer to bone: a fatal attraction *Nat. Rev. Cancer* **11** 411–25

[3] Roodman G D 2004 Mechanisms of bone metastasis *N Engl J Med.* **350** 1655–64

[4] Arrigoni C, Bersini S, Gilardi M and Moretti M 2016 *In vitro* co-culture models of breast cancer metastatic progression towards bone *Int. J. Mol. Sci.* **17** 1405

[5] Roca H and McCauley L K 2015 Inflammation and skeletal metastasis *Bonekey Rep.* **4** 706

[6] Lin Y, Xu J and Lan H 2019 Tumor-associated macrophages in tumor metastasis: biological roles and clinical therapeutic applications *J. Hematol. Oncol.* **12** 1–16

[7] Kusumbe A P 2016 Vascular niches for disseminated tumour cells in bone *J. Bone Oncol.* **5** 112–6

[8] Shay T, Jojic V, Zuk O, Rothamel K, Puyraimond-Zemmour D, Feng T, Wakamatsu E, Benoist C, Koller D and Regev A 2013 Conservation and divergence in the transcriptional programs of the human and mouse immune systems *Proc. Natl Acad. Sci. USA* **110** 2946–51

[9] Yamada K M and Cukierman E 2007 Modeling tissue morphogenesis and cancer in 3D *Cell* **130** 601–10

[10] Mcmillin D W, Negri J M and Mitsiades C S 2013 The role of tumour-stromal interactions in modifying drug response: challenges and opportunities *Nat. Rev. Drug Discovery* **12** 217–28

[11] Hoarau-Véchot J, Rafii A, Touboul C and Pasquier J 2018 Halfway between 2D and animal models: are 3D cultures the ideal tool to study cancer-microenvironment interactions? *Int. J. Mol. Sci.* **19** 181

[12] Bersini S, Arrigoni C, Lopa S, Bongio M, Martin I and Moretti M 2016 Engineered miniaturized models of musculoskeletal diseases *Drug Discov. Today* **21** 1429–36

[13] Clarke M S F, Sundaresan A, Vanderburg C R, Banigan M G and Pellis N R 2013 A three-dimensional tissue culture model of bone formation utilizing rotational co-culture of human adult osteoblasts and osteoclasts *Acta Biomater.* **9** 7908–16

[14] Bernhardt A, Thieme S, Domaschke H, Springer A, Rösen-Wolff A and Gelinsky M 2010 Crosstalk of osteoblast and osteoclast precursors on mineralized collagen-towards an *in vitro* model for bone remodeling *J. Biomed. Mater. Res.* A **95** 848–56

[15] Gershovich J G, Dahlin R L, Kasper F K and Mikos A G 2013 Enhanced osteogenesis in cocultures with human mesenchymal stem cells and endothelial cells on polymeric microfiber scaffolds *Tissue Eng.* A **19** 2565–76

[16] Correia C, Grayson W L, Park M, Hutton D, Zhou B, Guo X E, Niklason L, Sousa R A, Reis R L and Vunjak-Novakovic G 2011 *In vitro* model of vascularized bone: synergizing vascular development and osteogenesis *PLoS One* **6** e28352

[17] Dahlin R L, Gershovich J G, Kasper F K and Mikos A G 2014 Flow perfusion co-culture of human mesenchymal stem cells and endothelial cells on biodegradable polymer scaffolds *Ann. Biomed. Eng.* **42** 1381–90

[18] Pagani S, Torricelli P, Veronesi F, Salamanna F, Cepollaro S and Fini M 2018 An advanced tri-culture model to evaluate the dynamic interplay among osteoblasts, osteoclasts, and endothelial cells *J. Cell. Physiol.* **233** 291–301

[19] Forte L, Torricelli P, Boanini E, Gazzano M, Rubini K, Fini M and Bigi A 2016 Antioxidant and bone repair properties of quercetin-functionalized hydroxyapatite: an *in vitro* osteoblast-osteoclast-endothelial cell co-culture study *Acta Biomater.* **32** 298–308

[20] Bongio M, Lopa S, Gilardi M, Bersini S and Moretti M 2016 A 3D vascularized bone remodeling model combining osteoblasts and osteoclasts in a CaP nanoparticle-enriched matrix *Nanomedicine* **11** 1073–91

[21] James-Bhasin M, Siegel P M and Nazhat S N 2018 A three-dimensional dense collagen hydrogel to model cancer cell/osteoblast interactions *J. Funct. Biomater.* **9** 72

[22] Kim J *et al* 2018 Regulation of breast cancer-induced osteoclastogenesis by MacroH2A1.2 involving EZH2-Mediated H3K27me3 *Cell Rep.* **24** 224–37

[23] Popielarski M, Ponamarczuk H, Stasiak M, Watała C and Świątkowska M 2019 Modifications of disulfide bonds in breast cancer cell migration and invasiveness *Am. J. Cancer Res.* **9** 1554–82

[24] Binnemars-Postma K, Bansal R, Storm G and Prakash J 2018 Targeting the Stat6 pathway in tumor-associated macrophages reduces tumor growth and metastatic niche formation in breast cancer *FASEB J.* **32** 969–78

[25] Wyckoff J B, Wang Y, Lin E Y, Li J F, Goswami S, Stanley E R, Segall J E, Pollard J W and Condeelis J 2007 Direct visualization of macrophage-assisted tumor cell intravasation in mammary tumors *Cancer Res.* **67** 2649–56

[26] Hirt C, Papadimitropoulos A, Mele V, Muraro M G, Mengus C, Iezzi G, Terracciano L, Martin I and Spagnoli G C 2014 'In vitro' 3D models of tumor-immune system interaction *Adv. Drug Deliv. Rev.* **79** 145–54

[27] Bersini S, Gilardi M, Arrigoni C, Talò G, Zamai M, Zagra L, Caiolfa V and Moretti M 2016 Human *in vitro* 3D co-culture model to engineer vascularized bone-mimicking tissues combining computational tools and statistical experimental approach *Biomaterials* **76** 157–72

[28] Parlakian A, Gomaa I, Solly S, Arandel L, Mahale A, Born G, Marazzi G and Sassoon D 2010 Skeletal muscle phenotypically converts and selectively inhibits metastatic cells in mice *PLoS One* **5** e9299

[29] Lovitt C J, Shelper T B and Avery V M 2018 Doxorubicin resistance in breast cancer cells is mediated by extracellular matrix proteins *BMC Cancer* **18** 41

[30] Yellen P, Saqcena M, Salloum D, Feng J, Preda A, Xu L, Rodrik-Outmezguine V and Foster D A 2011 High-dose rapamycin induces apoptosis in human cancer cells by dissociating mTOR complex 1 and suppressing phosphorylation of 4E-BP1 *Cell Cycle* **10** 3948–56

[31] Moser G H, Schrader J and Deussen A 1989 Turnover of adenosine in plasma of human and dog blood *Am. J. Physiol. Cell Physiol.* **256** C799–806

[32] Hellsten Y, Maclean D, Rådegran G, Saltin B and Bangsbo J 1998 Adenosine concentrations in the interstitium of resting and contracting human skeletal muscle *Circulation* **98** 6–8

[33] Indraccolo S, Stievano L, Minuzzo S, Tosello V, Esposito G, Piovan E, Zamarchi R, Chieco-Bianchi L and Amadori A 2006 Interruption of tumor dormancy by a transient angiogenic burst within the tumor microenvironment *Proc. Natl Acad. Sci. USA* **103** 4216–21

[34] Bergers G and Benjamin L E 2003 Tumorigenesis and the angiogenic switch *Nat. Rev. Cancer* **3** 401–10

[35] Shimamura T, Amizuka N, Li M, Freitas P H L, White J H, Henderson J E, Shingaki S, Nakajima T and Ozawa H 2005 Histological observations on the microenvironment of osteolytic bone metastasis by breast carcinoma cell line *Biomed. Res.* **26** 159–72

[36] Labelle M and Hynes R O 2012 The initial hours of metastasis: the importance of cooperative host-tumor cell interactions during hematogenous dissemination *Cancer Discov.* **2** 1091–9

[37] Bersini S, Jeon J S, Dubini G, Arrigoni C, Chung S, Charest J L, Moretti M and Kamm R D 2014 A microfluidic 3D invitro model for specificity of breast cancer metastasis to bone *Biomaterials* **35** 2454–61

[38] Naumov G N *et al* 1999 Cellular expression of green fluorescent protein, coupled with high-resolution *in vivo* videomicroscopy, to monitor steps in tumor metastasis *J. Cell Sci.* **112** 1835–42

[39] Cserni G *et al* 2008 Variations in sentinel node isolated tumour cells/micrometastasis and non-sentinel node involvement rates according to different interpretations of the TNM definitions *Eur. J. Cancer* **44** 2185–91

[40] Heuzé-Vourc'h N *et al* 2005 IL-20, an anti-angiogenic cytokine that inhibits COX-2 expression *Biochem. Biophys. Res. Commun.* **333** 470–5

[41] Le Pape F, Vargas G and Clézardin P 2016 The role of osteoclasts in breast cancer bone metastasis *J. Bone Oncol.* **5** 93–5

[42] Ney J T, Fehm T, Juhasz-Boess I and Solomayer E F 2013 RANK, RANKL and OPG expression in breast cancer - influence on bone metastasis *Tumor Diagnostics & Therapy* **72** 385–91

[43] Renema N, Navet B, Heymann M F, Lezot F and Heymann D 2016 RANK-RANKL signalling in cancer *Biosci. Rep.* **36** e00366

[44] Deligiorgi M V, Panayiotidis M I, Griniatsos J and Trafalis D T 2020 Harnessing the versatile role of OPG in bone oncology: counterbalancing RANKL and TRAIL signaling and beyond *Clin. Exp. Metastasis* **37** 13–30

[45] Seibel M J 2005 Biochemical markers of bone turnover: part I: biochemistry and variability *Clin. Biochem. Rev.* **26** 97–122

[46] Awolaran O, Brooks S A and Lavender V 2016 Breast cancer osteomimicry and its role in bone specific metastasis; an integrative, systematic review of preclinical evidence *Breast* **30** 156–71

[47] Chiechi A, Novello C, Magagnoli G, Petricoin E F, Deng J, Benassi M S, Picci P, Vaisman I, Espina V and Liotta L A 2013 Elevated TNFR1 and serotonin in bone metastasis are correlated with poor survival following bone metastasis diagnosis for both carcinoma and sarcoma primary tumors *Clin. Cancer Res.* **19** 2473–85

[48] Steeland S, Libert C and Vandenbroucke R E 2018 A new venue of TNF targeting *Int. J. Mol. Sci.* **19** 1442

[49] García-Castro A *et al* 2015 APRIL promotes breast tumor growth and metastasis and is associated with aggressive basal breast cancer *Carcinogenesis* **36** 574–84

[50] Pelekanou V *et al* 2018 BCMA (TNFRSF17) induces APRIL and BAFF mediated breast cancer cell stemness *Front. Oncol.* **8** 301

[51] Mills C D, Kincaid K, Alt J M, Heilman M J and Hill A M 2000 M-1/M-2 Macrophages and the Th1/Th2 Paradigm *J. Immunol.* **164** 6166–73

[52] Murray P J *et al* 2014 Macrophage activation and polarization: nomenclature and experimental guidelines *Immunity* **41** 14–20

[53] Helm O, Held-Feindt J, Schäfer H and Sebens S 2014 M1 and M2: there is no 'good' and 'bad'-how macrophages promote malignancy-associated features in tumorigenesis *Oncoimmunology* **3** e946818

[54] Sousa S *et al* 2015 Human breast cancer cells educate macrophages toward the M2 activation status *Breast Cancer Res.* **17** 101

[55] Martinez F O, Sica A, Mantovani A and Locati M 2008 Macrophage activation and polarization *Front Biosci* **13** 453–61

[56] Zhang H, Tian L, Shen M, Tu C, Wu H, Gu M, Paik D T and Wu J C 2019 Generation of quiescent cardiac fibroblasts from human induced pluripotent stem cells for *in vitro* modeling of cardiac fibrosis *Circ. Res.* **125** 552–66

[57] Wessels D J *et al* 2019 Reciprocal signaling and direct physical interactions between fibroblasts and breast cancer cells in a 3D environment *PloS One* **14** e0218854

[58] Ghajar C M *et al* 2013 The perivascular niche regulates breast tumour dormancy *Nat. Cell Biol.* **15** 807–17

[59] Nguyen D X, Bos P D and Massagué J 2009 Metastasis: from dissemination to organ-specific colonization *Nat. Rev. Cancer* **9** 274–84

[60] Jeon J S, Bersini S, Gilardi M, Dubini G, Charest J L, Moretti M and Kamm R D 2015 Erratum: human 3D vascularized organotypic microfluidic assays to study breast cancer cell extravasation *Proc. Natl Acad. Sci. USA* **112** 214–9

[61] Fishman P, Bar-Yehuda S, Ohana G, Barer F, Ochaion A, Erlanger A and Madi L 2004 An agonist to the A3 adenosine receptor inhibits colon carcinoma growth in mice via modulation of GSK-3β and NF-κB *Oncogene* **23** 2465–71

[62] Rivankar S 2014 An overview of doxorubicin formulations in cancer therapy *J. Cancer Res. Ther.* **10** 853–8

[63] Li J, Kim S G and Blenis J 2014 Rapamycin: one drug, many effects *Cell Metab.* **19** 373–9

[64] Cappetta D, Rossi F, Piegari E, Quaini F, Berrino L, Urbanek K and De Angelis A 2018 Doxorubicin targets multiple players: a new view of an old problem *Pharmacol. Res.* **127** 4–14

[65] Barilli A *et al* 2008 In human endothelial cells rapamycin causes mTORC2 inhibition and impairs cell viability and function *Cardiovasc. Res.* **78** 563–71

[66] Son B, Lee S, Youn H S, Kim E G, Kim W and Youn B H 2017 The role of tumor microenvironment in therapeutic resistance *Oncotarget* **8** 3933–45

[67] Rao V A, Klein S R, Agama K K, Toyoda E, Adachi N, Pommier Y and Shacter E B 2009 The iron chelator Dp44mT causes DNA damage and selective inhibition of topoisomerase IIA in breast cancer cells *Cancer Res.* **69** 948–57

[68] Sonowal H, Pal P, Shukla K, Saxena A, Srivastava S K and Ramana K V 2018 Aldose reductase inhibitor, fidarestat prevents doxorubicin-induced endothelial cell death and dysfunction *Biochem. Pharmacol.* **150** 181–90

[69] Sun Y Z, Liu L, Cai N and Liu N N 2017 Anti-angiogenic effect of rapamycin in mouse oxygen-induced retinopathy is mediated through suppression of HIF-1alpha/VEGF pathway *Int. J. Clin. Exp. Pathol.* **10** 10167–75

[70] Cortini M, Baldini N and Avnet S 2019 New advances in the study of bone tumors: a lesson from the 3D environment *Front. Physiol.* **10** 814

[71] Krishnan V, Vogler E A, Sosnoski D M and Mastro A M 2014 *In vitro* mimics of bone remodeling and the vicious cycle of cancer in bone *J. Cell. Physiol.* **229** 453–62

[72] Villasante A, Marturano-Kruik A, Robinson S T, Liu Z, Guo X E and Vunjak-Novakovic G 2017 Tissue-engineered model of human osteolytic bone tumor *Tissue Eng.* C **23** 98–107

[73] De Peppo G M, Vunjak-Novakovic G and Marolt D 2014 Cultivation of human bone-like tissue from pluripotent stem cell-derived osteogenic progenitors in perfusion bioreactors *Methods Mol Biol* **1202** 173–84

[74] Francesca S, Veronica B, Silvia B, Gianluca G, Annapaola P, Simona C, Matteo C, Lucia M, Mazzotti A and Milena F 2016 An *in vitro* 3D bone metastasis model by using a human bone tissue culture and human sex-related cancer cells *Oncotarget* **7** 76966–83

[75] Quent V M C, Taubenberger A V, Reichert J C, Martine L C, Clements J A, Hutmacher D W and Loessner D 2018 A humanised tissue-engineered bone model allows species-specific breast cancer-related bone metastasis *in vivo* *J. Tissue Eng. Regen. Med.* **12** 494–504

[76] Zhou X, Zhu W, Nowicki M, Miao S, Cui H, Holmes B, Glazer R I and Zhang L G 2016 3D bioprinting a cell-laden bone matrix for breast cancer metastasis study *ACS Appl. Mater. Interfaces* **8** 30017–26

[77] Hao S, Ha L, Cheng G, Wan Y, Xia Y, Sosnoski D M, Mastro A M and Zheng S-Y 2018 A spontaneous 3D bone-on-a-chip for bone metastasis study of breast cancer cells *Small* **14** 1702787

[78] Sosa M S, Bragado P and Aguirre-Ghiso J A 2014 Mechanisms of disseminated cancer cell dormancy: an awakening field *Nat. Rev. Cancer* **14** 611–22

[79] Inoue K *et al* 2006 A crucial role for matrix metalloproteinase 2 in osteocytic canalicular formation and bone metabolism *J. Biol. Chem.* **281** 33814–24

[80] Morinobu M, Ishijima M, Rittling S R, Tsuji K, Yamamoto H, Nifuji A, Denhardt D T and Noda M 2003 Osteopontin expression in osteoblasts and osteocytes during bone formation under mechanical stress in the calvarial suture *in vivo J. Bone Miner. Res.* **18** 1706–15

[81] Pang X, Gong K, Zhang X, Wu S, Cui Y and Qian B Z 2019 Osteopontin as a multifaceted driver of bone metastasis and drug resistance *Pharmacol. Res.* **144** 235–44

[82] Bingle L, Brown N J and Lewis C E 2002 The role of tumour-associated macrophages in tumour progression: implications for new anticancer therapies *J. Pathol.* **196** 254–65

[83] Graney P L, Ben-Shaul S, Landau S, Bajpai A, Singh B, Eager J, Cohen A, Levenberg S and Spiller K L 2020 Macrophages of diverse phenotypes drive vascularization of engineered tissues *Sci. Adv.* **6** eaay6391

[84] Zenger S, He W, Ek-Rylander B, Vassiliou D, Wedin R, Bauer H and Andersson G 2011 Differential expression of tartrate-resistant acid phosphatase isoforms 5a and 5b by tumor and stromal cells in human metastatic bone disease *Clin. Exp. Metastasis* **28** 65–73

[85] Bersini S *et al* 2018 Engineering an environment for the study of fibrosis: a 3D human muscle model with endothelium specificity and endomysium *Cell Rep.* **25** 3858–68

[86] Fornetti J, Welm A L and Stewart S A 2018 Understanding the bone in cancer metastasis *J. Bone Miner. Res.* **33** 2099–113

[87] Madi L, Ochaion A, Rath-Wolfson L, Bar-Yehuda S, Erlanger A, Ohana G, Harish A, Merimski O, Barer F and Fishman P 2004 The A3 adenosine receptor is highly expressed in tumor versus normal cells: potential target for tumor growth inhibition *Clin. Cancer Res.* **10** 4472–9

[88] Brancato V, Kundu B, Oliveira J M, Correlo V M, Reis R L and Kundu S C 2020 Tumor-stroma interactions alter the sensitivity of drug in breast cancer *Front. Mater.* **7** 116